Chinese Journal of
POLYMER SCIENCE

RESEARCH ARTICLE

https://doi.org/10.1007/s10118-026-3665-y
Chinese J. Polym. Sci. **2026**, *44*, 2648–2658

Melanin-like Polylevodopa Nanoparticles with Enhanced UV-shielding Performance Using Benzoyl Peroxide

Sheng Long[a], Cheng Chang[a], Bei Zhou[a], Defa Hou[a], Xu Lin[a], and Yuan Zou[a,b*]

[a] *National Joint Engineering Research Center for Highly-Efficient Utilization Technology of Forestry Resources, Southwest Forestry University, Kunming 650224, China*
[b] *State Key Laboratory of Advanced Polymer Materials, Sichuan University, Chengdu 610065, China*

Electronic Supplementary Information

Abstract We report a bioinspired, facile strategy for synthesizing melanin-like nanoparticles *via* highly selective room-temperature polymerization of levodopa (*L*-DOPA), a native eumelanin precursor, using benzoyl peroxide. This method overcomes traditional synthesis limitations, yielding poly(*L*-DOPA) with covalently incorporated benzoyl fragments, and demonstrates significantly enhanced ultraviolet absorption for advanced photoprotective applications.

Keywords Biomimetic materials; Melanin; Benzoyl peroxide; Poly(*L*-DOPA); UV protection

Citation: Long, S.; Chang, C.; Zhou, B.; Hou, D. F.; Lin, X.; Zou, Y. Melanin-like polylevodopa nanoparticles with enhanced UV-shielding performance using benzoyl peroxide. *Chinese J. Polym. Sci.* **2026**, *44*, 2648–2658.

INTRODUCTION

Environmental concerns over ultraviolet (UV) radiation have spurred intense research into sustainable and biocompatible UV-protective materials. Nature offers a ubiquitous biopolymer, melanin, which is responsible for structural color, broadband light absorption, radical scavenging, and universal adhesion, ranging from plants to animals.[1–3] Inspired by natural melanin, a number of melanin-like polymers have been developed over the past decade.[4–6] Among them, polydopamine (PDA) has been the most popular eumelanin-like nanomaterial, playing an important role in biomedical,[7–9] energy,[10–13] and environmental applications.[14–16] However, regarding natural eumelanin, 5,6-dihydroxyindole-2-carboxylic acid (DHICA) is the dominant unit, which is almost absent in PDA.[4,17] There is a critical molecular discrepancy that the primary biosynthetic precursor to eumelanin is not dopamine but tyrosine which contains an additional carboxylic acid group. Levodopa (*L*-DOPA) serves as a class of fundamental building blocks that underpin the formation of high-performance biomaterials, such as melanin and mussel adhesive proteins.[18] Consequently, poly(*L*-DOPA) (P(*L*-DOPA)) represents a structurally more faithful and potentially functionally superior mimic of the native eumelanin.[19,20]

However, the existence of carboxyl groups within *L*-DOPA imposes several constraints on its oxidative polymerization process by reducing the nucleophilic reactivity of the amino group due to its electron-withdrawing effect.[21,22] Furthermore, DHICA, serving as the cyclization product of *L*-DOPA, provides fewer covalent bonding sites than DHI, while carboxyl ionization under mild alkaline conditions may also hinder its self-assembly process.[4] Traditional synthetic approaches, such as thermal treatment or the use of strong chemical oxidants, often lead to non-selective over-oxidation or poorly controlled polymer structures, thereby limiting the performance of the resulting materials.[23–26] These challenges underscore the need for a mild, selective initiation method that can not only drive the polymerization of *L*-DOPA, but also preserve and potentially enhance its intrinsic optical functionality. Benzoyl peroxide (BPO), a common radical initiator that is widely used in vinyl polymerization, has emerged as a potential candidate for this purpose.[27,28] BPO can induce the oxidation of polyphenolic compounds, such as tea polyphenols, into quinone derivatives, thereby diminishing or eliminating their antioxidant activity.[29] Notably, the role of BPO in *L*-DOPA polymerization is mechanistically distinct from its conventional function in vinyl systems. Although BPO initiates vinyl polymerization *via* radical addition to double bonds, in the present system, it promotes oxidative polymerization through hydrogen abstraction from the catechol moiety of *L*-DOPA.[29,30] This mechanistic distinction is critical for understanding the unique efficacy of BPO in constructing melanin-like poly(*L*-DOPA) materials with enhanced UV-shielding performance.

Herein, we developed a straightforward yet highly effective chemical strategy to address these limitations, as illustrated in Fig. 1(a). Through systematic screening of organic per-

* Corresponding author, E-mail: yzou24@swfu.edu.cn
Received January 6, 2026; Accepted March 12, 2026; Published online May 14, 2026

oxides, BPO was identified as a uniquely efficient initiator for room-temperature oxidative polymerization of *L*-DOPA in a benign aqueous solvent mixture. BPO undergoes clean homolytic cleavage to generate phenyl radicals that selectively initiate polymerization.[31–33] The success of this approach is intimately linked to the zwitterionic nature of *L*-DOPA under weakly acidic conditions. This "self-locked" conformation, stabilized by an intramolecular hydrogen bond, prevents the ammonium group from acting as a radical trap and directs the initiator specifically toward the catechol ring, enabling efficient and controlled chain propagation. This BPO-initiated route avoids the need for complex enzymatic systems or harsh oxidants and provides a robust, scalable, and cost-effective synthetic pathway. The resulting poly(*L*-DOPA) exhibited a tailored energy bandgap, influenced by the incorporation of benzoyl-derived motifs and a higher proportion of uncyclized *L*-DOPA units, leading to significantly enhanced ultraviolet absorption properties. This work advances the synthesis of next-generation, performance-driven, melanin-inspired materials by providing a fundamental chemical

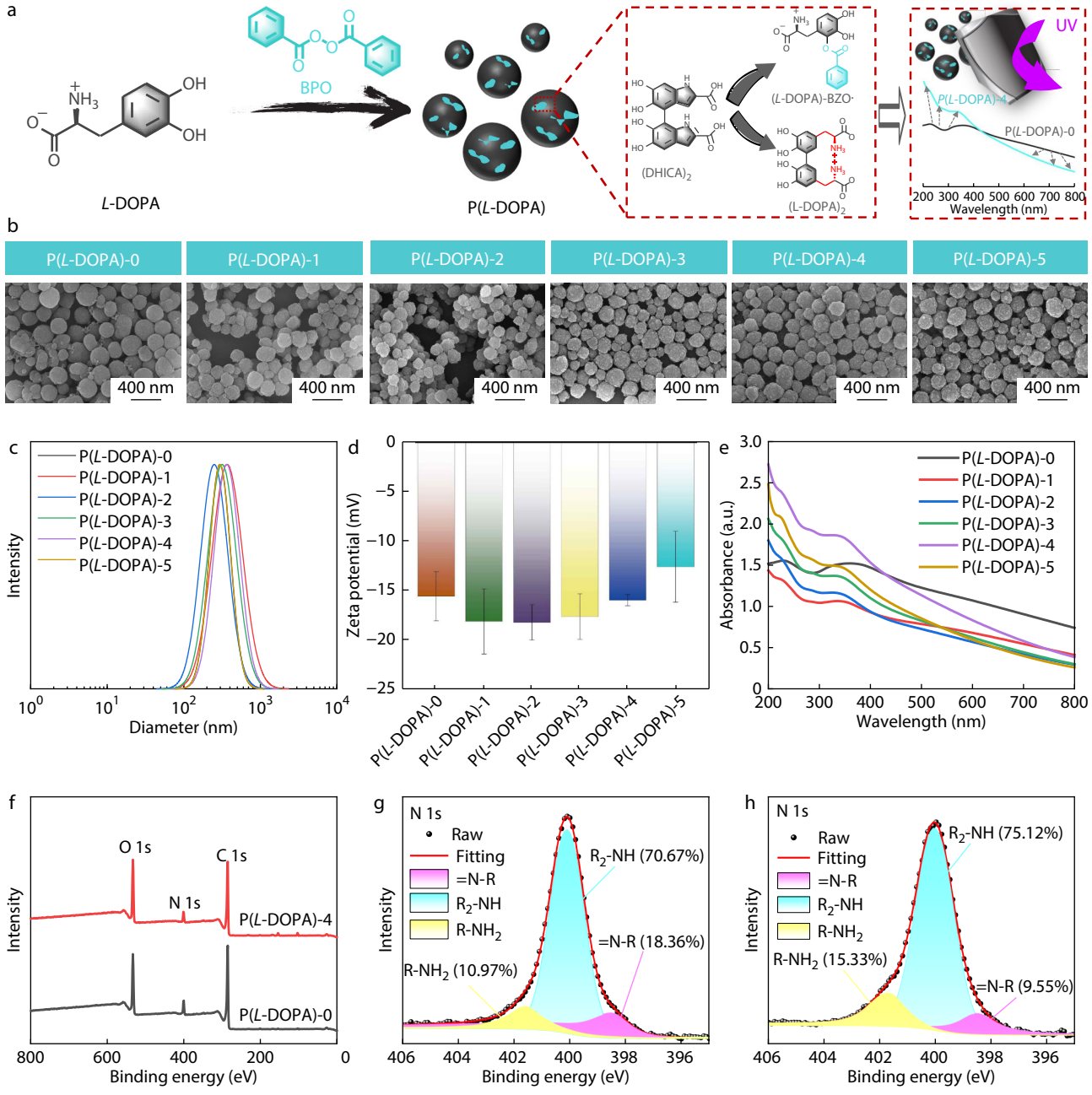

Fig. 1 Synthesis and characterization of P(*L*-DOPA) NPs. (a) Schematic illustration of BPO-mediated enhanced ultraviolet protection poly(*L*-DOPA) nanoparticle synthesis; (b) SEM images of P(*L*-DOPA)-*i* (*i*=0 to 5); (c) Hydrodynamic size of P(*L*-DOPA)-*i* (*i*=0 to 5) NPs determined by DLS; (d) Zeta potential of P(*L*-DOPA)-*i* (*i*=0 to 5) NPs; (e) UV-Vis absorption spectra of P(*L*-DOPA)-*i* (*i*=0 to 5) NPs. The concentration of the test solution is 50 ug/mL. (f) XPS spectra of P(*L*-DOPA)-0 and P(*L*-DOPA)-4; (g) N 1s peaks in the XPS spectra of P(*L*-DOPA)-0; (h) N 1s peaks in the XPS spectra of P(*L*-DOPA)-4.

https://doi.org/10.1007/s10118-026-3665-y

methodology that directly addresses the long-standing challenge of *L*-DOPA polymerization, opening avenues for their application in advanced coatings and photoprotective systems.

EXPERIMENTAL

Materials

3,4-Dihydroxy-*L*-phenylalanine (*L*-DOPA) (99%), dopamine hydrochloride (98%), tert-butyl hydroperoxide (70%), tert-butyl peroxide (98%), 2,5-bis(tert-butylperoxy)-2,5-dimethylhexane (93%), 1,1-di(tert-butylperoxy) cyclohexane (80%), di(tert-butylperoxyisopropyl) benzene (96%), tert-butyl peroxybenzoate (TBPB) (98%), 3-chloroperoxybenzoic acid (*m*-CPBA) (85%), benzoyl peroxide (BPO) (75%), acetonitrile (99%), 3,4-dihydroxybenzoic acid (98%), Rhodamine B (99%), tetrabutylammonium hexafluorophosphate (Bu_4NPF_6) (99%), ferrocene (99%), Titanium dioxide (TiO_2) (99%), poly(vinyl alcohol) (98 mol%–100 mol%, 32–45 mPa·s) were purchased from Adamas Reagents Co., Ltd. (Shanghai, China). Acetone (99%), were purchased from Shandian Pharmaceutical Co., Ltd. (Kun Ming, China). All the chemical reagents were used directly without further purification. Deionized water was used in all the experiments.

Characterization

Scanning electron microscope (SEM) images of the PDA coatings were obtained using ZEISS Sigma 300. The test mode was backscattered electron mode, and the test voltage was 15 kV. X-ray photoelectron spectroscopy (XPS) was conducted with an Escalab 250Xi (Thermo Scientific, USA) using Al-Kα radiation. Avantage software was used to analyze the survey scan XPS spectra using adventitious carbon to standardize the C 1s binding energy (284.8 eV). UV-Vis absorption and transmittance spectra were obtained using a UV-Vis light spectrophotometer (SHIMADZU, UV-2600). Dynamic light scattering (DLS) and zeta potential measurements were performed using a 90 PLUS PALS Nano Brook particle analyzer, and all the samples were measured in aqueous solutions (pH=7). The electrospray ionization mass spectrometry (ESI-MS) spectrum of the crude reaction was measured by Shimadzu LCMS-IT-TOF using the positive ion mode ESI. The XRD spectra of the films were obtained using an Anton Paar XRDynamic500 instrument. The measured spectral range was 200–800 nm with a slit of 1 nm. Furthermore, the water contact angles were tested using a YP-JC1 with an 8 μL water drop. CV measurements were performed using a CHI760E electrochemical workstation. This test was completed using P(*L*-DOPA) coatings coated with Indium Tin Oxide conductive glass as the working electrode, Pt wire as the counter electrode, and Ag/AgCl as the reference electrode in a 0.1 mol/L Bu_4NPF_6 acetonitrile solution. The Fc/Fc^+ couple was used as an internal reference. Also, the thermal stability of samples before and after UV irradiation was evaluated by using thermogravimetric analysis (TGA, HQG-3) tests from room temperature (25 °C) to 800 °C at a ramp rate of 10 °C/min under nitrogen atmosphere. The mechanical behavior of the samples was tested using a universal testing machine (ZQ-990LB) at a strain rate of 2 mm/min. The average value of the three samples was measured for each measurement. The width of the tested film was 2 mm, with an average thickness of (0.12±0.01) mm.

Theoretical Calculations

The energy levels of the molecular orbits and the ESPs were obtained using density functional theory (DFT) using Gaussian 09 software. The molecular orbits of probable intermediates were output at the B3LYP/6-31G (d) level with solvation model density (SMD).

Reaction pathway translation was obtained by DFT using the Gaussian 09 software. The molecular orbits of the probable intermediates were output at the B3LYP/ 6-311++G (2d, p) level with SMD.

Synthesis of P(*L*-DOPA)-0

600 mg (3.04 mmol) of *L*-DOPA was added to 150 mL of deionized water, stirred under heating at 75 °C for 24 h, and centrifuged three times with deionized water to obtain similarly sized P(*L*-DOPA).

Synthesis of P(*L*-DOPA)-1 to P(*L*-DOPA)-5

Different amounts of BPO (261.5 mg, 1.08 mmol; 523.0 mg, 2.16 mmol; 784.4 mg, 3.24 mmol; 1046.0 mg, 4.32 mmol; 1307.4 mg, 5.4 mmol) were fully dissolved in 120 mL of acetone with magnetic stirring for 20 min. *L*-DOPA 213 mg (1.08 mmol) was dissolved in 40 mL of deionized water at 50 °C, allowed to cool to room temperature, and then quickly injected into the above solution. After stirring for 24 h, similarly sized P(*L*-DOPA) was obtained by centrifugation (once with acetone solution and twice with deionized water).

Synthesis of P(*L*-DOPA)-6

133 μL (0.71 mmol) was fully dissolved in 42 mL of acetone solution with magnetic stirring for 20 min. *L*-DOPA 140 mg (0.71 mmol) was dissolved in 40 mL of deionized water at 50 °C, allowed to cool to room temperature, and then quickly injected into the above solution. After stirring for 24 h, P(*L*-DOPA) was obtained by centrifugation (once with acetone solution and twice with deionized water).

Synthesis of P(*L*-DOPA)-7

172.6 mg (0.71 mmol) of *m*-CPBA was fully dissolved in 42 mL of acetone with magnetic stirring for 20 min. *L*-DOPA 140 mg (0.71 mmol) was dissolved in 40 mL of deionized water at 50 °C, allowed to cool to room temperature, and then quickly injected into the above solution. After stirring for 24 h, similarly sized P(*L*-DOPA) was obtained by centrifugation (once with acetone solution and twice with deionized water).

Fabrication of P(*L*-DOPA)@PVA Film

PVA (10 g) was added to 100 mL of deionized water. The PVA solution was stirred at 80 °C until completely dissolved. The solution was cooled to room temperature for later use.

PVA solution (10 mL of the PVA solution was poured into a disposable Petri dish with a diameter of 90 mm. Then, it was placed in an oven at 60 °C under windless conditions and dried for three days to obtain a pure PVA film.

One milliliter of the previously prepared aqueous dispersions of P(*L*-DOPA)-0 and P(*L*-DOPA)-4 nanoparticles was taken and freeze-dried. The dried nanoparticles were weighed and the concentration of P(*L*-DOPA) in the original dispersions was calculated accordingly.

From the well-dispersed P(*L*-DOPA) nanoparticle solutions with known concentrations, aliquots corresponding to 4 mg of polymer were withdrawn for subsequent experiments.

https://doi.org/10.1007/s10118-026-3665-y

Each aliquot was separately mixed with 10 mL of a homogeneous PVA solution and stirred for 1 h. The mixtures were then poured into disposable Petri dishes (90 mm in diameter). The dishes were placed in an oven at 60 °C under windless conditions and dried for 3 days to obtain P(*L*-DOPA)-0@PVA film and P(*L*-DOPA)-4@PVA films.

UV Photocatalytic Dye Degradation by Films

First, 200 mL of an aqueous solution of Rhodamine B (Rh B) with a concentration of 20.9 mmol/L was prepared. Subsequently, 20 mg of titanium dioxide (TiO_2) was added, and the mixture was stirred in the dark for 30 min. Subsequently, Petri dishes containing freshly prepared 20.9 mmol/L Rh B solution were covered with PVA, P(*L*-DOPA)-0@PVA, and P(*L*-DOPA)-4@PVA films.

The photocatalytic degradation efficiency was investigated under ultraviolet (UV) light at a wavelength of 365 nm. It should be noted that the distance from the UV lamp to the surface of the solution was maintained at 8 cm. After irradiation for *t* minutes, 1.5 mL of the solution was collected from the petri dish and centrifuged. The absorption of the Rh B solution at 552 nm was measured using a UV-Vis spectrophotometer. The photocatalytic degradation efficiency under UV light was calculated using the equation $I = (1 - A_t/A_0) \times 100\%$, where A_0 represents the absorption of the Rh B solution without UV exposure, and at denotes the absorption after t min of UV irradiation. In addition, dye degradation in the same system was examined in the dark as a control.

RESULTS AND DISCUSSION

Initially, systematic screening of alkyl, aralkyl, acyl, and substituted aroyl peroxides for *L*-DOPA polymerization revealed that only benzoyl-containing peroxides were effective. After mixing *L*-DOPA with different peroxides, BPO demonstrated superior reactivity, yielding the darkest product within 8 h (Fig. S1 in the electronic supplementary information, ESI). Density functional theory (DFT) calculations of the highest occupied molecular orbital and lowest unoccupied molecular orbital of the reagents were performed to elucidate this specificity and were listed in Fig. S2 (in ESI). *L*-DOPA has a high HOMO (–5.54 eV), while non-benzoyl peroxides possess high LUMO levels, creating a large gap for electron transfer. The benzoyl group critically lowered the LUMO of the peroxide (*e.g.*, BPO's LUMO is –1.53 eV), enabling efficient electron acceptance from *L*-DOPA. Although 3-chloroperoxybenzoic acid shares an identical LUMO (–1.53 eV), its higher HOMO (–6.94 eV versus BPO's –7.10 eV) and non-radical reaction pathway limit its efficacy. Additionally, the symmetric structure of BPO is critical, as its homolytic cleavage generates two phenyl radicals *via* decarboxylation, maximizing the initiation efficiency and accounting for its optimal performance. The experimental results also supported this reactive activity. After 24 h of reaction, the sample oxidized by tert-butyl peroxybenzoate exhibited stronger absorption than that treated with 3-chloroperoxybenzoic acid, confirming that BPO is the optimal oxidant for subsequent experiments. The monomeric forms of BPO, *L*-DOPA, tert-butyl peroxybenzoate, and 3-chloroperoxybenzoic acid exhibited absorption confined to wavelengths below 300 nm (Fig. S4 in ESI).

Building upon the selective efficacy of BPO in initiating *L*-DOPA polymerization established earlier, BPO was employed here as an efficient oxidant to synthesize a series of poly(*L*-DOPA) nanoparticles. A series of poly(*L*-DOPA) nanoparticles was prepared by varying the molar ratio of *L*-DOPA to BPO (1:1, 1:2, 1:3, 1:4, and 1:5), and the resulting nanoparticles were denoted as poly(*L*-DOPA)-*i* (*i*=1–5), respectively. For comparison, a control sample, poly(*L*-DOPA)-0, was also synthesized *via* a thermal oxidation method without using BPO. According to scanning electron microscopy (SEM) and dynamic light scattering (DLS) measurements, the diameters of all the samples were approximately (188±16) nm, indicating the spherical morphology and uniform size of the as-prepared poly(*L*-DOPA) samples (Fig. 1b). Dynamic light scattering (DLS) analysis revealed that all P(L-DOPA) samples possessed a monomodal size distribution with low polydispersity, confirming the formation of uniform nanoparticles. The Z-average hydrodynamic diameters were centered primarily in the range of 200–400 nm (Fig. 1c). The SEM-EDS mapping showed that poly(*L*-DOPA) had three elements, C, N, and O, which were uniformly distributed within the nanoparticles (Fig. S5 in ESI). The zeta potential values of each sample are summarized in Fig. 1(d), with average values of approximately -16.4 mV, revealing the relatively stable suspension of the samples in aqueous dispersions.

A comparison between P(*L*-DOPA)-0 and the BPO-oxidized series P(*L*-DOPA)-*i* (*i*=1–5) showed that the BPO-derived samples exhibited composition-dependent optical properties. With an increase in the BPO ratio, the UV absorption progressively increased, with a maximum at sample P(*L*-DOPA)-4, exhibiting the most pronounced enhancement across the entire UV region, and slightly decreased at P(*L*-DOPA)-5. (Fig. 1e). The integrated UV absorption (200–400 nm) enhancement of the BPO-oxidized P(*L*-DOPA)-*i* samples was –25.44%, –16.29%, –1.98%, 32.28%, 8.77%. for *i*=1 to 5, respectively, compared to the control P(*L*-DOPA)-0. The initial decrease at low BPO ratios (*i*=1–3) can be attributed to the disruption of the conjugated polymer backbone at the early stages of modification, while as the BPO loading further increased, the incorporated benzoyl-derived fragments began to function as intrinsic chromophores to effectively enhance UV absorption and reach a maximum at P(L-DOPA)-4. However, at the highest BPO loading (*i*=5), the over-incorporation of benzoyl fragments may disrupt polymer chain packing or induce structural defects that partially compromise conjugation efficiency, leading to a slight decrease in UV absorption. Additionally, it is noteworthy that BPO-mediated polymerization resulted in a decrease in absorption in the visible and near-infrared regions (Fig. 1e). We propose that this modified absorption profile, characterized by enhanced UV absorption and reduction at longer wavelengths, originates from the incorporation of BPO-derived fragments. These fragments are hypothesized to function as intrinsic chromophores and tailor the energy-band structure of the polymer. To elucidate the potential incorporation of benzoyl peroxide (BPO) fragments into the poly(*L*-DOPA) architecture, Fourier transform infrared spectroscopy (FTIR), X-ray photoelectron spectroscopy (XPS), and electrospray ionization mass spectrometry (ESI-MS) were conducted to elucidate the potential incorporation of BPO fragments into the poly(L-DOPA) architecture. The FTIR spectra of both BPO-oxidized poly(*L*-DOPA)-0 and poly(*L*-DOPA)-4 ex-

hibited nearly identical profiles, featuring characteristic absorptions at approximately 3150 cm^{-1} (O—H stretching), 1715 cm^{-1} (C=O stretching), and 1624 cm^{-1} (aromatic C=C vibrations) (Fig. S6 in ESI). No distinct new bands were detected upon BPO initiation, as the carbonyl (C=O) and aromatic signals of pristine BPO at 1755 and 1593 cm^{-1} were not present as separate peaks but were likely obscured within the broad, overlapping vibrational modes of the polymeric backbone, suggesting no significant introduction of new types of functional groups. The XPS survey spectra confirmed the presence of C 1s, N 1s, and O 1s core-level signals in both poly(*L*-DOPA)-0 and poly(*L*-DOPA)-4 (Fig. 1f). Quantitative analysis revealed slight yet notable differences in the elemental composition. High-resolution C 1s spectra could be deconvoluted into four consistent components for both samples, which were C=C (284.5 eV), C—C (285.1 eV), C—OH/C—N (286.1 eV), and C=O (288.9 eV) (Fig. S7 in ESI).[14,34] The N 1s spectrum could be deconvoluted into three components for both samples: $-NH_2$ (401.7 eV), —NH— (400.1 eV), and —N= (398.5 eV).[35] The N 1s spectra featured contributions from the pyrrolic nitrogen and amine species in both polymers. The increase in amine species from 10.97% (P(*L*-DOPA)-0) to 15.33% (P(*L*-DOPA)-4) indicated a higher content of uncyclized *L*-DOPA monomers (Figs. 1g and 1h). The enlarged uncyclized fraction shortens the effective conjugation length, resulting in a blue shift in absorption toward the UV region, consequently reducing visible light absorption.[20] Notably, the high-resolution O 1s analysis provided semi-quantitative evidence that a substantially higher proportion of C=O species existed in poly(*L*-DOPA)-4 than in the control, which can be rationally attributed to the covalent incorporation of benzoate-derived moieties originating from the BPO fragmentation during the initiation step.

This study systematically elucidated the decomposition and reaction mechanisms of BPO through integrated experimental and theoretical analyses. Fig. 2(a) presents the time-dependent radical concentration profile obtained using 4-hydroxy-2,2,6,6-tetramethylpiperidine-1-oxyl (TEMPO) as a spin-trapping agent,[31] where a drastic increase in signal intensity confirms the rapid homolytic cleavage of BPO under the reaction conditions, generating active radical intermediates. Supporting this, the DFT-based free-energy calculations in Fig. 2(b) map the preferred reaction pathway. The initial binding interaction between the phenolic hydroxyl group of L-DOPA and the carbonyl moiety of BPO entails an increase in free energy of 24.27 kcal/mol. Subsequently, the formation of *L*-DOPA-quinone (*L*-DQZ) coupled with the cleavage of BPO into benzoic acid and a benzoyloxyl radical (BzO·) is strongly favored, exhibiting a significant free energy drop to −18.90 kcal/mol, indicating the thermodynamic feasibility of this key step. Critically, ESI-MS analysis provided direct evidence of the covalent integration of BPO fragments into oligomeric structures (Fig. 2c). Key fragments were identified, including a dimeric species at *m/z*=407, corresponding to [2DHICA +

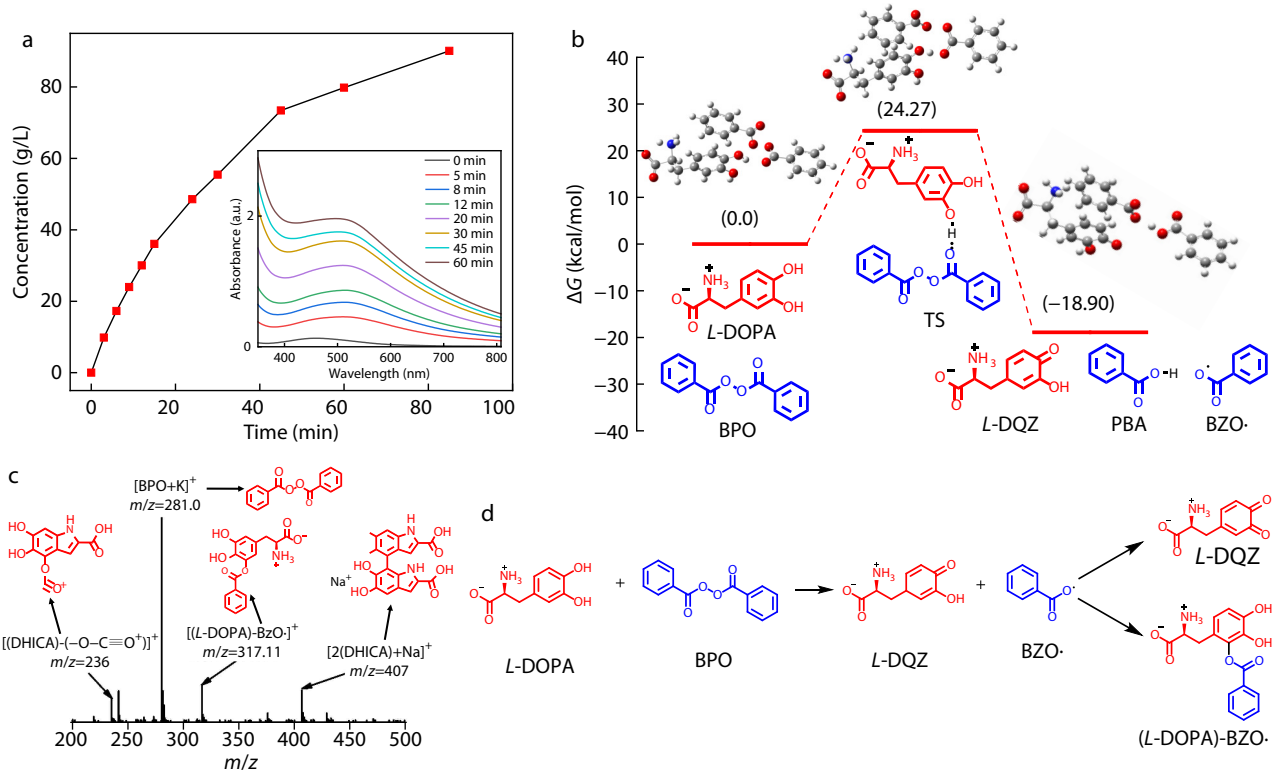

Fig. 2 Verification of reaction mechanisms. (a) Evolution of benzoyloxyl radical concentration over varying ultrasound irradiation times. Inset: UV-Vis absorption spectra of BzO-TEMPO recorded as a function of sonication time. (b) Free energy difference curve in the reaction process of *L*-DOPA and benzoyl peroxide. Free energies are in units of kcal/mol and calculated at the B3LYP/ 6-311++G (2d, p) level with solvation model density (SMD). (c) ESI-MS spectrum of the crude product solution after 30 min reaction; (d) Possible oxidation pathways of *L*-DOPA and the generation and doping pathways of benzoyloxyl radicals.

Na]$^+$, and several adducts, such as [IQ-BzO + K]$^+$ (m/z=308.0) and [DHICA-BzO + K]$^+$ (m/z=354.7), where BzO represents the benzoyloxy ($C_6H_5C(O)O$—) group. These fragments unambiguously confirm that the homolytic cleavage of the BPO—O bond generates reactive radicals that covalently couple with *L*-DOPA-derived intermediates (*e.g.*, DHI and DHICA), thereby initiating and propagating polymerization. Fig. 2(d) illustrates the reaction pathway from the initial BPO homolytic cleavage to final polymer formation. This demonstrates the generation of the key benzoyloxyl radical intermediate and its subsequent coupling with *L*-DOPA-derived species to form primary adducts, followed by the progression of these oligomers through cross-coupling and chain growth into poly(*L*-DOPA).

Above all, the combined spectroscopic and spectrometric evidence confirms that BPO serves not only as an efficient initiator for *L*-DOPA polymerization under mild conditions, but also as a source of benzoyloxyl radicals that become covalently embedded within the polymer architecture, rationalizing its distinct composition and superior efficacy compared to thermal oxidation alone.

Mechanism of the Light Harvesting Ability

The optoelectronic and mechanistic basis for the enhanced UV absorption was investigated through combined experimental and computational analyses. The HOMO/LUMO energy levels were estimated from the onset oxidation and reduction potentials using the equation ELUMO/HOMO = $-e$ ($E_{ox/red}$ + 4.40) eV, where the potential of the Fc/Fc$^+$ couple was measured to be 0.40 V versus Ag/AgCl (Fig. S8 in ESI). Electrochemical bandgap measurements using this approach revealed a significant difference between the materials, with P(*L*-DOPA)-0 exhibiting a bandgap of 0.89 eV, while the BPO-derived P(*L*-DOPA)-4 showed a notably larger bandgap of 1.3 eV (Figs. 3a and 3b). The increased bandgap of P(*L*-DOPA)-4 directly blue-shifts its absorption edge, leading to enhanced UV absorption and reduced absorption in the visible region. Notably, when dopamine was used instead of *L*-DOPA with BPO, the reaction produced only an orange-yellow solution with oligomers, in contrast to the rapid formation of a dark polymer observed with *L*-DOPA, highlighting the critical role of the chemical structure of the monomer in polymerization efficiency, as shown in Fig. 3(c). This empirical finding was rationalized by electrostatic potential analysis, and possible chemical structures were theoretically investigated using DFT calculations performed at the B3LYP/6-31G (d) level of theory. The calculations demonstrated that in its zwitterionic state, *L*-DOPA's ammonium and carboxylate groups of *L*-DOPA formed a self-locked structure, effectively deactivating the amino group (Fig. 3d). In contrast, the exposed cationic amino group in dopamine readily quenches the electrophilic benzoyloxyl radicals from BPO,[36,37] suppressing polymerization. DFT simulations were performed on the key oligomeric models to bridge the molecular structure with macroscopic absorption (Fig. 3e). Based on the O 1s and N 1s XPS analyses, which revealed the coexistence of uncyclized *L*-DOPA units, cyclized/quinoid structures, and covalently incorporated benzoyloxy fragments, five representative oligomeric models were constructed to investigate their electronic properties. The results show that cyclized structures, particularly the quinoid form M2 with a bandgap of 1.88 eV, possess a significantly reduced bandgap compared to their non-cyclized counterpart M4 (2.30 eV). This trend holds for phenolic forms as well (M1:4.10 eV versus M3:4.84 eV), confirming that cyclization and quinone formation, both central outcomes of the BPO-mediated oxidation, are processes that intrinsically lower the optical bandgap. Furthermore, the model incorporating the benzoyloxy moiety exhibited a bandgap of 4.20 eV. While this specific

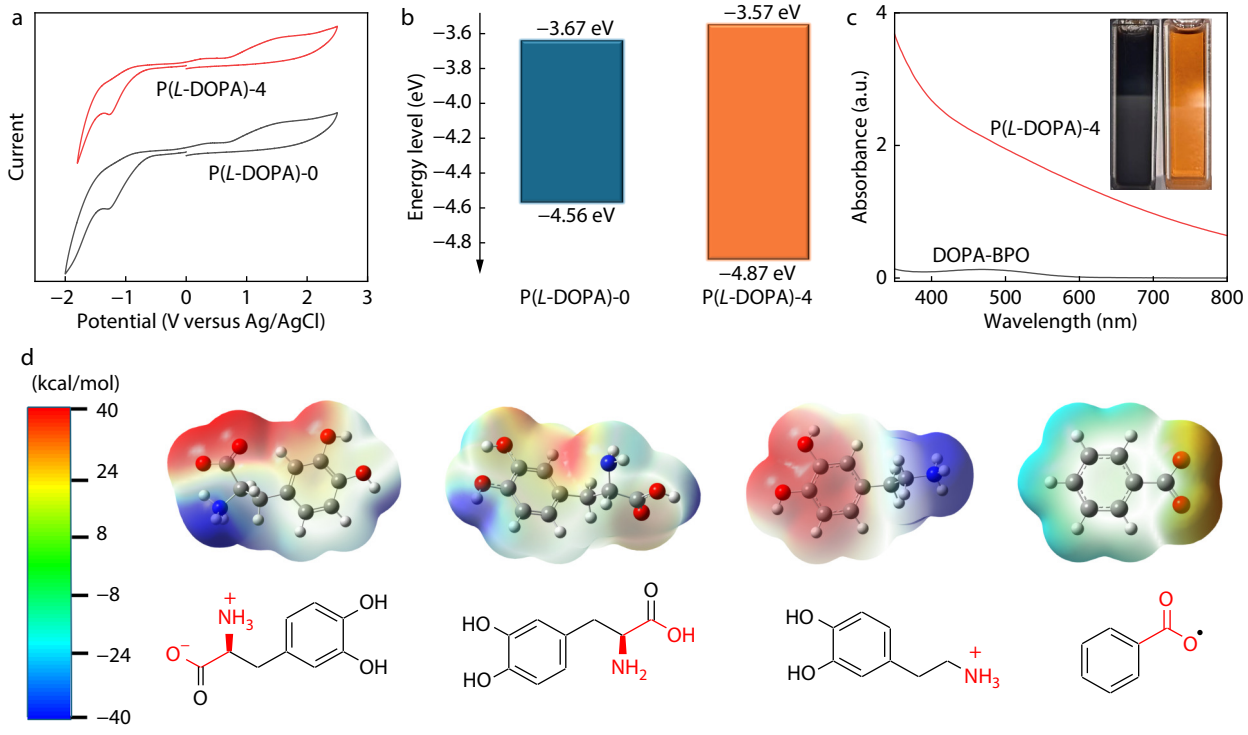

https://doi.org/10.1007/s10118-026-3665-y

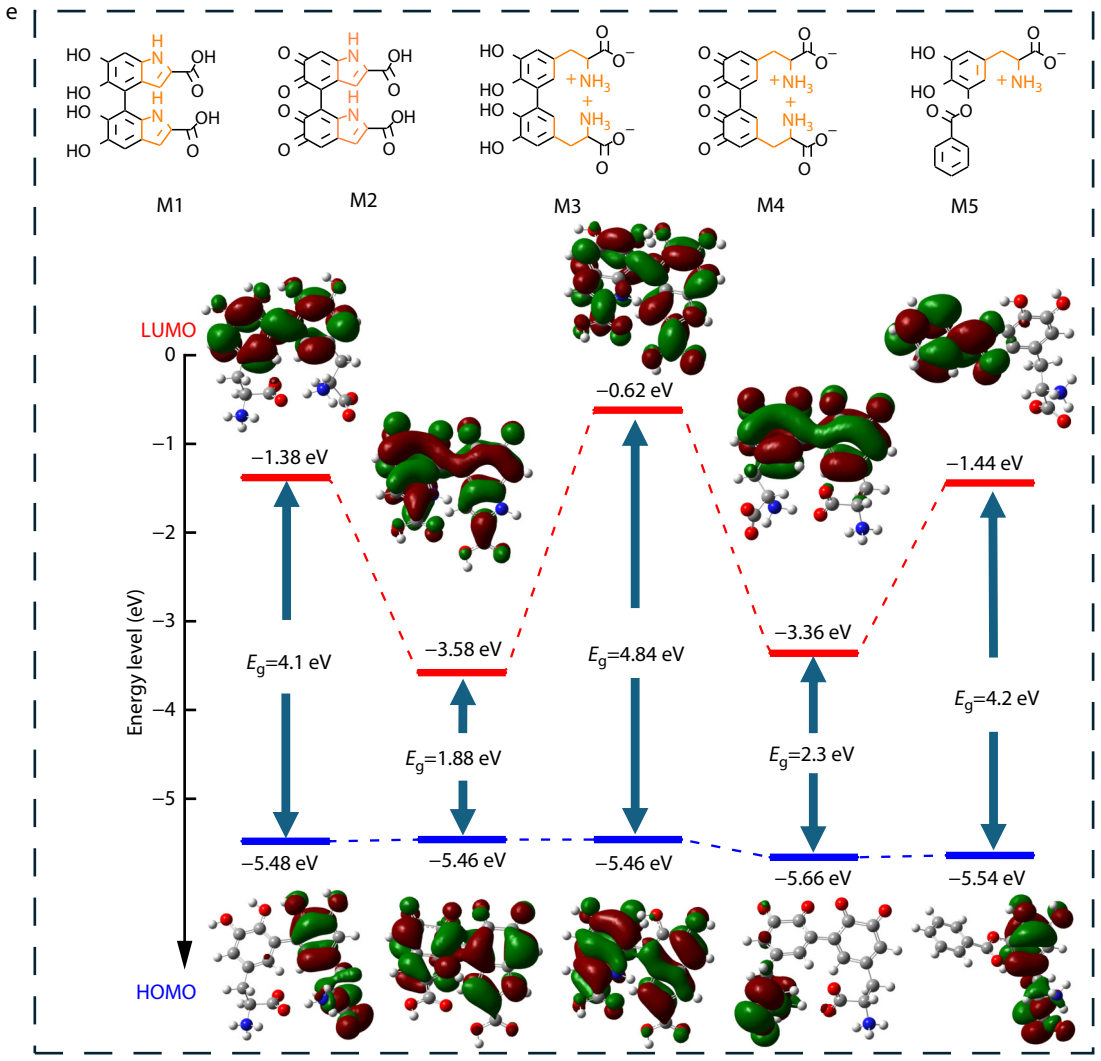

Fig. 3 Reasoning for the enhancement of ultraviolet absorption. (a) CVs of P(*L*-DOPA)-0 and P(*L*-DOPA)-4; (b) Schematic illustration of the energy levels of P(*L*-DOPA)-0 and P(*L*-DOPA)-4; (c) UV-Vis absorption spectra of P(*L*-DOPA)-4 and DOPA-BPO. UV-Vis absorbance and photographs of dopamine solutions were measured after being diluted fourfold. (d) Chemical structures of related monomers with ESP; (e) Chemical structures of possible intermediates within the PDA microstructure and frontier molecular orbital using DFT calculations at the B3LYP/6-31G* level with solvation model density. The possible intermediate fragments during polymerization, namely M1−M5.

adduct may not be the primary UV chromophore, the ensemble of simulation data strongly indicates that the BPO-initiated reaction pathway efficiently drives *L*-DOPA toward the formation of low-bandgap cyclized/quinoid oligomeric units. The larger electrochemical bandgap of P(*L*-DOPA)-4 compared to that of P(*L*-DOPA)-0 likely reflects a more ordered or electronically distinct structure arising from this controlled radical-initiated process. Therefore, the superior UV absorption is conclusively attributed to a synergistic effect: the unique efficacy of BPO in selectively polymerizing *L*-DOPA, combined with the inherent electronic structure of the cyclized conjugated oligomeric products.

UV Protection of P(*L*-DOPA) Films

The UV-shielding composite films were fabricated by incorporating P(*L*-DOPA) nanoparticles into a PVA matrix, where hydrogen-bonding interactions ensure strong interfacial integration (Fig. 4a). While the pure PVA film was transparent, the composite films P(*L*-DOPA)-0@PVA and P(*L*-DOPA)-4@PVA exhibited a dark brown color, with the former appearing darker, which is consistent with their different synthetic origins. The corresponding SEM images show that the incorporation of nanoparticles introduced discernible surface roughness to the otherwise smooth PVA film (Figs. 4b–4d). FTIR spectra confirmed successful incorporation, showing new characteristic bands at approximately 3277 cm^{-1} (attributed to N—H stretching from P(*L*-DOPA)) and 1726 cm^{-1} (assigned to C=O stretching from quinone or benzoyloxy groups) in the composites, which were absent in pure PVA (Fig. 4e).

XRD analysis revealed that all the samples had a broad peak near 20°, indicating a semi-crystalline structure (Fig. 4f). However, the introduction of P(*L*-DOPA) reduced the overall crystallinity of PVA, suggesting its role as a structural disruptor that interferes with the orderly packing of the PVA chains. Mechanical testing revealed that pure PVA exhibited high toughness but softness, with a fracture strain of 62% and a relatively low tensile strength of 22.8 MPa (Fig. 4g). In con-

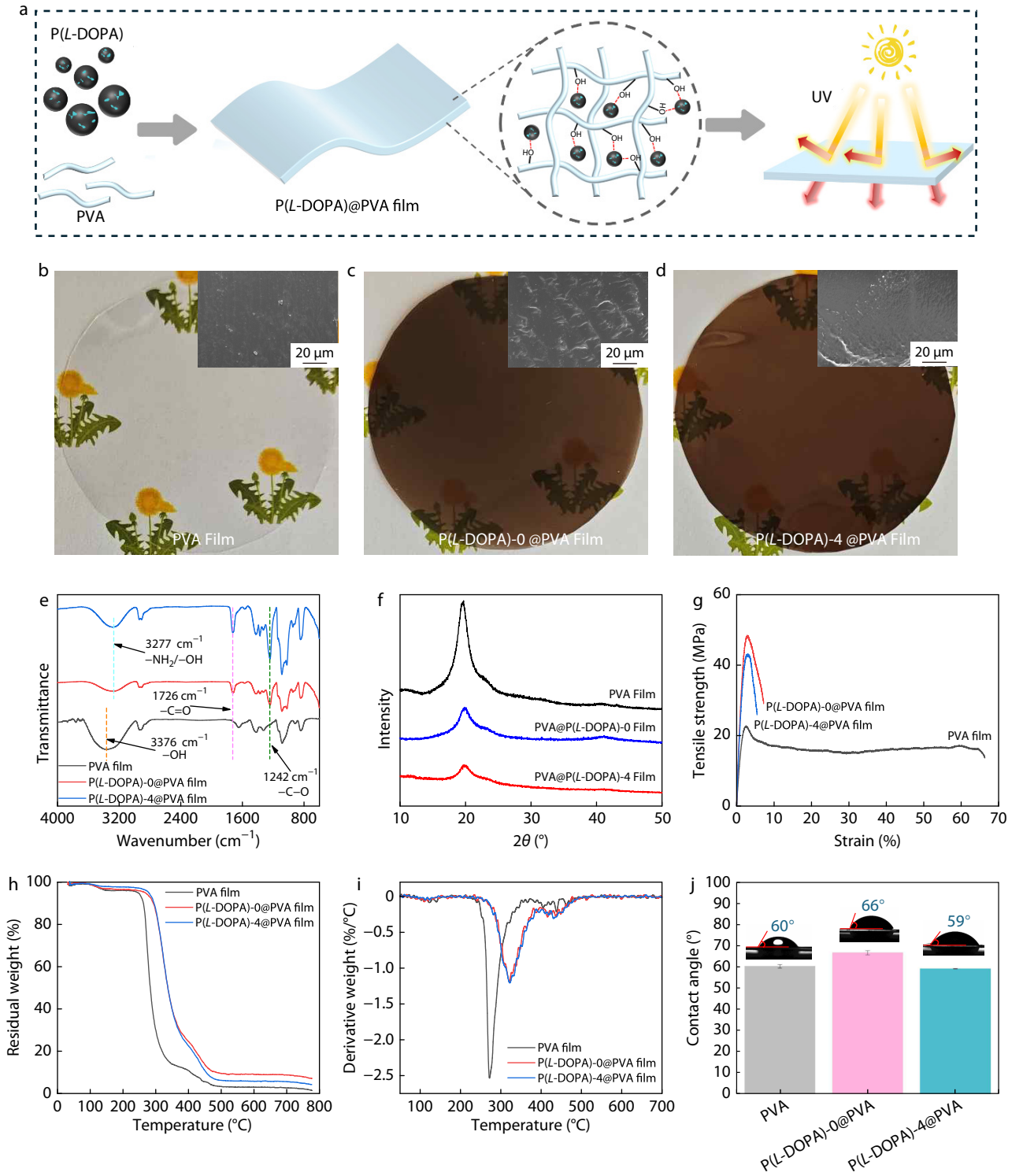

Fig. 4 Synthesis and performance characterization of PVA composite films. (a) Schematic of the preparation process for PVA composite films. (b–d) Optical photographs and SEM images of PVA composite films; (e) ATR-FTIR, (f) XRD, (g) stress-strain, (h) TG and (i) DTG spectra of PVA film, P(*L*-DOPA)-0@PVA film and P(*L*-DOPA)-4@PVA film; (j) Water contact angles of PVA film, P(*L*-DOPA)-0@PVA film and P(*L*-DOPA)-4@PVA film.

trast, both composite films demonstrated significantly enhanced strengths. Their tensile strengths increased markedly, reaching 48.3 MPa for P(*L*-DOPA)-0@PVA and 42.5 MPa for P(*L*-DOPA)-4@PVA, despite their fracture strain being below 10% (Fig. S9 in ESI). This transition from ductile to brittle mechanical behavior is attributed to the dense hydroxyl (—OH) groups on the PVA chains, which form strong hydrogen bonds with the catechol/phenolic moieties of P(*L*-DOPA). Such "chemical hooks" substantially strengthen the interfacial adhesion between particles and matrix, enabling efficient

stress transfer across the particle -PVA interface under tension and thereby leading to the notable improvement in tensile strength.[14,38] TGA results demonstrated that P(*L*-DOPA) incorporation enhanced the thermal stability of PVA (Fig. 4h). The temperatures at 5% weight loss for PVA, P(*L*-DOPA)-0@PVA, and P(*L*-DOPA)-4@PVA were 245.20, 267.89, and 278.47 °C, respectively. The DTG curves showed that the main decomposition peak for PVA was at 271.62 °C, whereas the peaks for the composite films were slightly weaker and broader, suggesting a retarded thermal degradation process (Figs. 4h and 4i). The water contact angles of the PVA, P(*L*-DOPA)-0@PVA, and P(*L*-DOPA)-4@PVA films were 60°, 66°, and 59°, respectively, indicating a moderately hydrophilic surface with minor variations (Fig. 4j). These results collectively demonstrate that the incorporation of P(*L*-DOPA) effectively improves the toughness and thermal stability of PVA. The balanced mechanical and thermal properties, along with retained hydrophilicity, provide a suitable material foundation for developing functional films for UV-protective applications.

UV-Vis transmittance spectra showed that pure PVA film had a high transmittance above 400 nm (exceeding 90%) but it offered little protection in the UV region (200–400 nm). In contrast, the composite films strongly absorbed the UV light. The average transmittances in the UV region for P(*L*-DOPA)-0@PVA and P(*L*-DOPA)-4@PVA were about 11.1% and 8.0%, respectively. Notably, P(*L*-DOPA)-4@PVA achieved a higher average transmittance (about 42.1%) in the visible-near infrared region compared to P(*L*-DOPA)-0@PVA (about 33.7%), indicating its superior ability to selectively block harmful UV radiation while maintaining better visibility, as shown in Figs. 5(a) and 5(b). In a practical Rhodamine B (RhB) dye degradation test under 20 W 365 nm UV light, the films were used as protective covers. After 10 min, the dye solution covered by P(*L*-DOPA)-4@PVA retained its highest concentration (about 71.8%), demonstrating the best shielding effect. Even after prolonged exposure for 50 min, a significant amount of dye (about 27.3%) remained in the P(*L*-DOPA)-4@PVA film (Fig. 5c). As shown in Fig. 5(d), after 50 min of UV irradiation, the Rhodamine B solution capped with the P(L-DOPA)-4@PVA film exhibited the highest absorbance at 545 nm, reaching 0.098, whereas the solution covered with the pure PVA film showed a significantly lower value of 0.022. Finally, the UV indicator card test provided visual evidence. After exposure, the card protected by the P(*L*-DOPA)-4@PVA film exhibited a slight color change, similar to an unexposed blank card, whereas the card under pure PVA exhibited a color change comparable to that with no cover (Fig. 5e). Subsequently, the blackness of the cards was quantified. As shown in Fig. 5(f), the card protected by the P(L-DOPA)-4@PVA film exhibited the highest blackness value of 84.64. In comparison, the card protected by the P(L-DOPA)-0@PVA film afforded a slightly lower value of 78.35. Notably, the card coated with the pure PVA film showed a negligible protective effect, with a blackness of 59.83, which was nearly identical to that of the unprotected card (59.71). This series of experiments confirmed that the P(*L*-DOPA)-4@PVA composite film acts as an efficient and

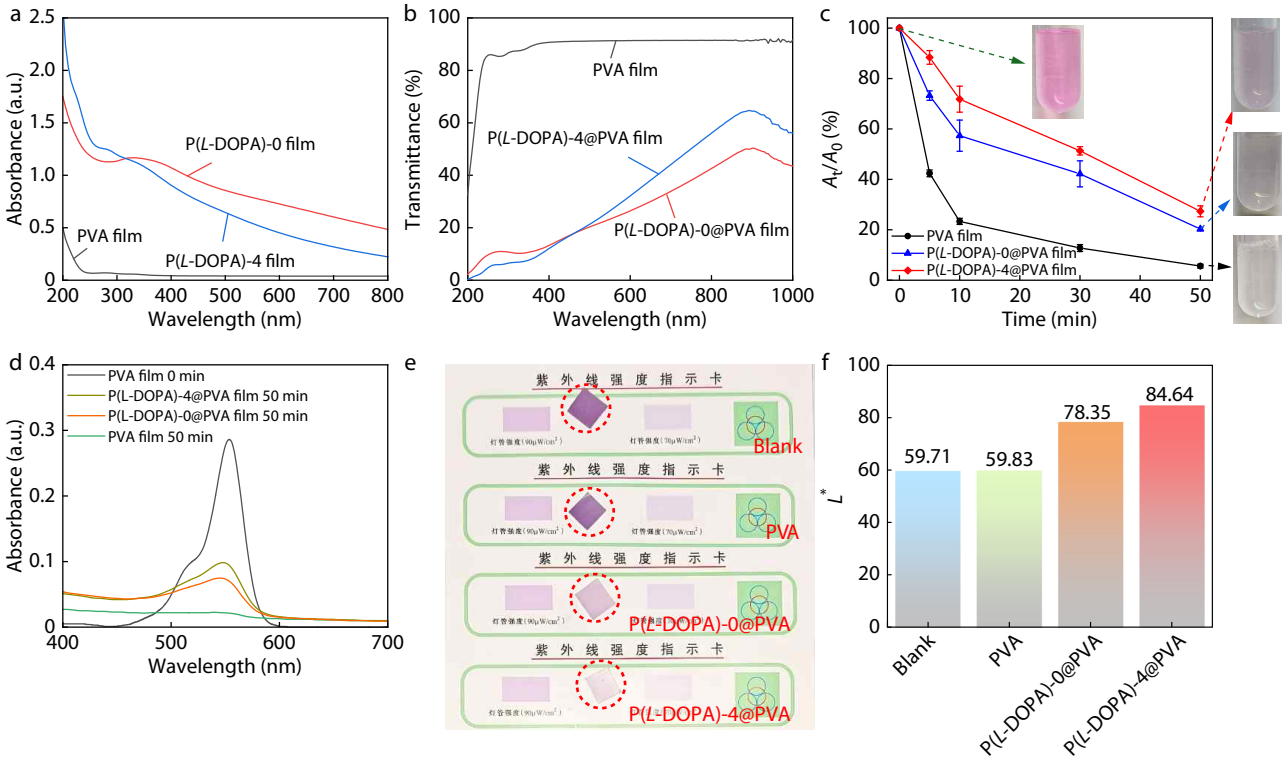

Fig. 5 Ultraviolet resistance. (a) UV-Vis absorption and (b) transmittance spectra of PVA composite films; (c) Photodegradation curves of Rh B solutions protected by PVA composite films. (inset: original Rh B solution, solution covered by PVA film, P(*L*-DOPA)-0@PVA film and P(*L*-DOPA)-4@PVA film.) (d) UV-Vis absorption spectra of Rh B solution Under different irradiation times; (e) Photos of color changes in UV intensity indicator cards after 3 min of irradiation under both PVA composite film-covered and uncovered conditions; (f) Contrast of darkness after color development of ultraviolet intensity indicator card.

https://doi.org/10.1007/s10118-026-3665-y

selective UV filter, offering robust protection against UV damage while allowing greater transmission of visible light, which is desirable for practical applications requiring both optical clarity and UV protection.

CONCLUSIONS

In summary, this study established a simple and efficient biomimetic strategy for synthesizing advanced melanin-like materials by controlling the oxidative polymerization of *L*-DOPA under mild conditions using BPO as a specific radical initiator. This unique efficacy originates from a synergistic mechanism, where benzoyl-derived radicals selectively initiate polymerization, while the intrinsic zwitterionic form of *L*-DOPA directs the pathway to favor chain propagation, as confirmed by mass spectrometry and computational simulation. This tailored polymerization could fabricate poly(*L*-DOPA) nanomaterials with an increased optical bandgap (from 0.89 eV to 1.3 eV) and significantly enhanced UV absorption, achieving up to a 47% improvement in shielding performance. Furthermore, when fabricated into PVA composite films, the materials demonstrated not only superior UV-shielding performance, exhibiting a low average UV transmittance of about 8.0%, but also improved toughness and thermal stability. Thus, by providing fundamental mechanistic insight, this study offers a versatile platform for designing next-generation bio-inspired materials with customized optoelectronic and protective properties for various applications.

Conflict of Interests

The authors declare no interest conflict.

Electronic Supplementary Information

Electronic supplementary information (ESI) is available free of charge in the online version of this article at http://doi.org/10.1007/s10118-026-3665-y.

Data Availability Statement

The data supporting the findings of this study are available from the author upon request. E-mail: yzou24@swfu.edu.cn.

ACKNOWLEDGMENTS

This work was financially supported by the Youth Foundation of Yunnan Province (No. 202501AU070046), the Programs of Science and Technology Department of Yunnan Province (No. YNQR-QNRC-2018-099), and the Opening Project of the State Key Laboratory of Advanced Polymer Materials, Sichuan University (No. sklapm2025-3-32).

REFERENCES

1 D'Alba, L.; Shawkey, M. D. Melanosomes: biogenesis, properties, and evolution of an ancient organelle. *Physiol. Rev.* **2019**, *99*, 1–19.
2 Xiao, M.; Hu, Z.; Wang, Z.; Li, Y.; Tormo, A. D.; Le Thomas, N.; Wang, B.; Gianneschi, N. C.; Shawkey, M. D.; Dhinojwala, A. Bioinspired bright noniridescent photonic melanin supraballs. *Sci. Adv.* **2017**, *3*, e1701151.
3 Xie, W.; Dhinojwala, A.; Gianneschi, N. C.; Shawkey, M. D. Interactions of melanin with electromagnetic radiation: from fundamentals to applications. *Chem. Rev.* **2024**, *124*, 7165–7213.
4 Cao, W.; Zhou, X. H.; McCallum, N. C.; Hu, Z. Y.; Ni, Q. Z.; Kapoor,

Graphical Abstract

Melanin-like Polylevodopa Nanoparticles with Enhanced UV-shielding Performance Using Benzoyl Peroxide

Sheng Long, Cheng Chang, Bei Zhou, Defa Hou, Xu Lin, and Yuan Zou

Southwest Forestry University; Sichuan University

This study presents a biomimetic strategy for efficiently synthesizing polylevodopa (poly(*L*-DOPA)) nanoparticles using benzoyl peroxide, yielding materials with tailored electronic structures and significantly enhanced UV-shielding performance for advanced protective coatings.

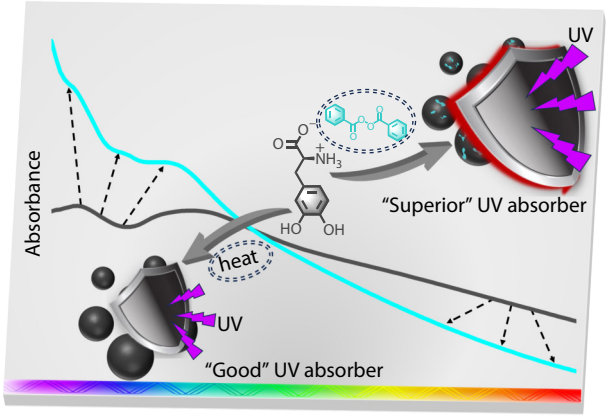

U.; Heil, C. M.; Cay, K. S.; Z. T.; Mantanona, A. J.; A. Jayaraman.; A. Dhinojwala.; D. Deheyn.; M. Shawkey.; M. Burkart.; J. D. Rinehart.; N. Gianneschi. Unraveling the structure and function of melanin through synthesis. *J. Am. Chem. Soc.* **2021**, *143*, 2622–2637.
5 Xu, Y. T.; Hu, J. F.; Hu, J. J.; Cheng, Y. Y.; Chen, X. C.; Gu, Z. P.; Li, Y. W. Bioinspired polydopamine hydrogels: strategies and applications. *Prog. Polym. Sci.* **2023**, *146*, 101740.
6 Yang, P.; Zhu, F.; Zhang, Z. B.; Cheng, Y. Y.; Wang, Z.; Li, Y. W. Stimuli-responsive polydopamine-based smart materials. *Chem. Soc. Rev.* **2021**, *50*, 8319–8343.
7 Wang, C.; Zhang, R.; Zhang, J. H.; Zhang, X. Q.; Zhang, H. J.; Cao, H.; Yang, Z.; Li, Y. W. Synthetic fungal melanin UV absorbers. *Sci. China Chem.* **2024**, *67*, 3098–3110.
8 Yang, P.; Gu, Z.; Zhu, F.; Li, Y. Structural and functional tailoring of melanin-like Polydopamine radical scavengers. *CCS Chem.* **2020**, *2*, 128–138.
9 Yang, Z.; Wang, X. H.; Bai, W. J.; Zou, Z. K.; Wu, H. X.; Li, Y. W. Structural disruption of melanin-like polymers with boosted UV protection. *Sci. China Chem.* **2024**, *67*, 1653–1663.
10 Chen, P.; He, S.; Wang, T.; Wang, C.; Tao, J.; Li, Y. Melanin-like nanofibers with highly ordered structures achieve ultrahigh specific electromagnetic interference shielding efficiency. *Nat. Commun.* **2025**, *16*, 7127.
11 Li, N.; Zhang, X. Q.; Zhu, J. Y.; Xiong, S. H.; Xu, Y. T.; Li, Y. W. Bioinspired flexible composite hydrogels for efficient solar steam generation and stable electricity harvest. *Nano Lett.* **2025**, *25*, 10072–10081.
12 Pei, C. Y.; Zhang, H. J.; Li, Y. W.; Gu, Z. P.; Chen, X. C.; Kuang, T. R. Robust and durable biodegradable polymer-based triboelectric nanogenerators enabled by trace amounts of melanin-like nanoparticles. *Nano Energy* **2025**, *135*, 18893–18900.
13 Yang, P.; Wang, T. Y.; Zhang, J. H.; Zhang, H. J.; Bai, W. J.; Duan, G. G.; Zhang, W.; Wu, J. R.; Gu, Z. P.; Li, Y. W. Manipulating the antioxidative capacity of melanin-like nanoparticles by involving condensation polymerization. *Sci. China Chem.* **2023**, *66*, 1520–1528.
14 Bai, W. J.; Liang, B.; Luo, B. G.; Wang, J. Y.; Zhang, H. J.; Zhang, X. Q.; Yang, L.; Xu, Y. T.; Li, Y. W. Ultra-High bromine removal from waste water and downstream high-value utilization using melanin-like polymers. *Small* **2025**, *21*, 2410496.
15 Zou, Y.; Chen, X.; Yang, P.; Liang, G.; Yang, Y.; Gu, Z.; Li, Y. Regulating the absorption spectrum of polydopamine. *Sci. Adv.* **2020**, *6*, eabb4696.
16 Zou, Y.; Liu, H. J.; Wang, X. H.; Xu, Y. T.; Yang, Y.; Bai, W. J.; Li, Y. W. Light harvesting modulation of melanin-like polymers *via* Thiol-Michael "click" chemistry. *Macromolecules* **2023**, *56*, 9530–9539.
17 Ito, S. Reexamination of the structure of eumelanin. *Biochim. Biophys. Acta, Gen. Subj.* **1986**, *833*, 155–161.
18 Sivasundarampillai, J.; Youssef, L.; Priemel, T.; Mikulin, S.; Eren, E. D.; Zaslansky, P.; Jehle, F.; Harrington, M. J. A strong quick-release biointerface in mussels mediated by serotonergic cilia-based adhesion. *Science* **2023**, *382*, 829–834.
19 Wang, X.; Zhang, J.; Li, H.; Zhang, R.; Yang, X.; Li, W.; Li, Z.; Gu, Z.; Li, Y. Quaternary ammonium assisted synthesis of melanin-like poly(L-DOPA) nanoparticles with a boosted photothermal effect. *ACS Appl. Mater. Interfaces* **2024**, *16*, 22493–22503.
20 Wang, X.; Zhang, J.; Yang, L.; Wang, T.; Duan, G.; Gu, Z.; Li, Y. Eumelanin-like poly(levodopa) nano scavengers for inflammation disease therapy. *Biomacromolecules* **2024**, *25*, 2563–2573.
21 C. Tan.; C. D. Rudd.; A. J. Parsons.; N. Sharmin.; I. Ahmed. L-DOPA coating improved phosphate glass fibre strength and fibre/matrix interface. *J. Mech. Behav. Biomed. Mater.* **2022**, *136*, 105480.
22 Tesoro, C.; Lelario, F.; Ciriello, R.; Bianco, G.; Di Capua, A.; Acquavia, M. A. An overview of methods for L-DOPA extraction and analytical determination in plant matrices. *Separations* **2022**, *9*, 224.
23 Kirby, G. W.; Ogunkoya, L. Structure of melanin derived from (±)-3,4-dihydroxy-[14C, 3H] phenylalanine by oxidation with tyrosinase. *Chem. Commun.* **1965**, *21*, 546–547.
24 Strube, O. I.; Büngeler, A.; Bremser, W. Site-Specific in situ synthesis of eumelanin nanoparticles by an enzymatic autodeposition-like process. *Biomacromolecules* **2015**, *16*, 1608–1613.
25 Wang, T. Y.; Fan, Q. Q.; Hong, J.; Chen, Z.; Zhou, J. H.; Dai, Y. Q.; Jiang, H.; Gu, Z. P.; Cheng, Y. Y.; LI, Y. W. Therapeutic nanoparticles from grape seed for modulating oxidative stress. *Small* **2021**, *17*, 2102485.
26 Wang, T. Y.; Zhang, J. H.; Chen, Z.; Zhang, R.; Duan, G. G.; Wang, Z.; Chen, X. C.; Gu, Z. P.; Li, Y. W. sonochemical synthesis of natural polyphenolic nanoparticles for modulating oxidative stress. *Small* **2024**, *20*, 2401731.
27 Duan, J. J.; Huang, Y. Q.; Wei, F. Q.; Gao, Y.; Wan, F. S.; Feng, J. C. Processability and structure of dynamically modified linear low-density polyethylene with different branching contents using a high peroxide content. *Chinese J. Polym. Sci.* **2026**, *44*, 87–99.
28 Wang, W. J.; Huang, C. H.; Guo, Z. X.; Yu, J. Preparation of POE/PS blends with fine particle sizes by diffusion and subsequent polymerization of styrene in POE pellets. *J. Polym. Sci.* **2017**, *35*, 939–949.
29 Liu, Y.; Shangguan, L.; Zhao, B.; Chen, B.; Shi, B.; Wang, Y. Cross-linked supramolecular polymer networks constructed by pillar[5]arene-based host–guest recognition and coordination/oxidation of catechol. *Polym. Chem.* **2022**, *13*, 3763–3767.
30 Li, F. M.; Chen, S. J.; Li, Z. C.; Qiu, J. Vinyl monomers bearing chromophore moieties and their polymers—X. initiation and photochemical properties of p-(*N*,*N*-dimethylamino) styrene and its polymers. *Chinese J. Polym. Sci.* **1999**, *17*, 563–570.
31 Batten, J. J. 573. Structural effects in the reaction between benzoyl peroxide and phenols. *J. Chem. Soc.* **1956**, 2959-2966.
32 Cosgrove, S. L.; Waters, W. A. 670. The oxidation of phenols with benzoyl peroxide. *J. Am. Chem. Soc.* **1949**, 3189–3194.
33 Denney, D. B.; Denney, D. Z. Studies of the mechanisms of the reactions of benzoyl peroxide with secondary amines and phenols. *J. Am. Chem. Soc.* **1960**, *82*, 1389–1393.
34 Wang, Z.; Wang, Z.; Pan, X.; Fu, L.; Lathwal, S.; Olszewski, M.; Yan, J.; Enciso, A. E.; Wang, Z.; Xia, H and K. Matyjaszewski. Ultrasonication-Induced aqueous atom transfer radical polymerization. *ACS Macro Lett.* **2018**, *7*, 275–280.
35 Tan, L.; Zhu, T.; Huang, Y.; Yuan, H.; Shi, L.; Zhu, Z.; Yao, P.; Zhu, C.; Xu, J. Ozone-Induced rapid and green synthesis of polydopamine coatings with high uniformity and enhanced stability. *Adv. Sci.* **2024**, *11*, 2308153.
36 Kim, K. W.; Thomas, R. L. Antioxidative activity of chitosans with varying molecular weights. *Food Chem.* **2007**, *101*, 308–313.
37 Okamoto, K.; Ohkubo, K.; Kadish, K. M.; Fukuzumi, S. Remarkable accelerating effects of ammonium cations on electron-transfer reactions of quinones by hydrogen bonding with semiquinone radical anions. *J. Phys. Chem. A.* **2004**, *108*, 10405–10413.
38 Yang, Z.; Zhang, J.; Liu, H.; Hu, J.; Wang, X.; Bai, W.; Zhang, W.; Yang, Y.; Gu, Z.; Li, Y. A bioinspired strategy toward UV absorption enhancement of melanin-like polymers for sun protection. *CCS Chem.* **2023**, *5*, 2389–2402.